Supplement of Solid Earth, 17, 537–554, 2026
https://doi.org/10.5194/se-17-537-2026-supplement

Solid Earth Open Access EGU

Supplement of

Impact of differential stress on fracture due to volume increasing hydration

Jeremiah J. McElwee et al.

Correspondence to: Jeremiah J. McElwee (mcelw020@umn.edu)

S1 Inferring Young's Moduli from the Stress-Strain Curves

To quantify the macroscopic properties (**Table 1)** that result from the microscopic parameters described in the Methods section, we performed uniaxial compression and tension test simulations (**Fig. S1**). These simulations were run on models made up of 0% reacted and 100% reacted disks. Plane strain was assumed when calculating elastic parameters from the simulations. To calculate Young's modulus, the tangent of the initial slope of the stress-strain curves was used so as to match dynamic Young's moduli calculated from acoustic experiments (*Christensen, 2004*) and because the DEM does not exhibit noise during initial loading, as is commonly a concern in laboratory experiments. For details on how the uniaxial compression and tension simulations are conducted, and for how stress and strain is measured in these simulations, see *Okamoto and Shimizu (2015)* and *Shimizu and Okamoto (2016).* The obtained macroscopic properties values (**Table 1**) are in good agreement with those reported by *Okamoto and Shimizu (2015)* and *Shimizu and Okamoto (2016).*

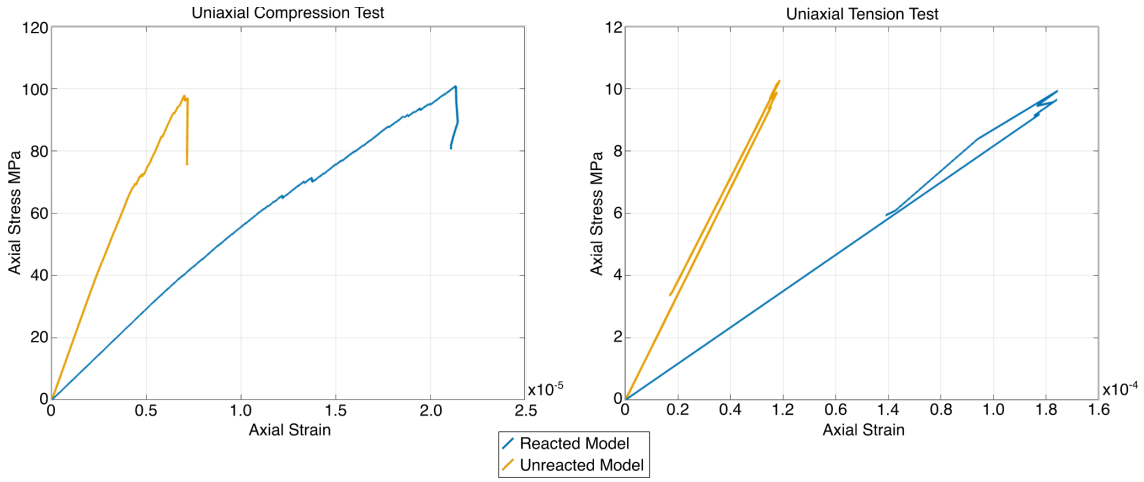

Figure S1: Stress-strain relations for plots of models with reacted disks (blue lines) and unreacted disks (blue lines) models subjected to (a) uniaxial compression and (b) uniaxial tension.

S2 Effect of Initial Disk Packing

In the simulations presented in this study, disks are initially randomly packed into the model domain. Previous work indicates that the variance in model behaviour in uniaxial compression, uniaxial tension, and brazil tests arising from different initial disk packing arrangements is small but is inversely dependent on the number of disks (*Shimizu et al., 2010*). In this study, we use 3151 disks, which is intermediate relative to similar studies (*Zhang et al., 2019; Shimizu and Okamoto, 2016; Okamoto and Shimizu, 2015*). An additional pair of simulations under horizontal deviatoric compression and tension indicate that the results are similar for a different initial packing then displayed in **Figs 3–6** in the main text (**Fig. S2**). Although there are slight variations in the main

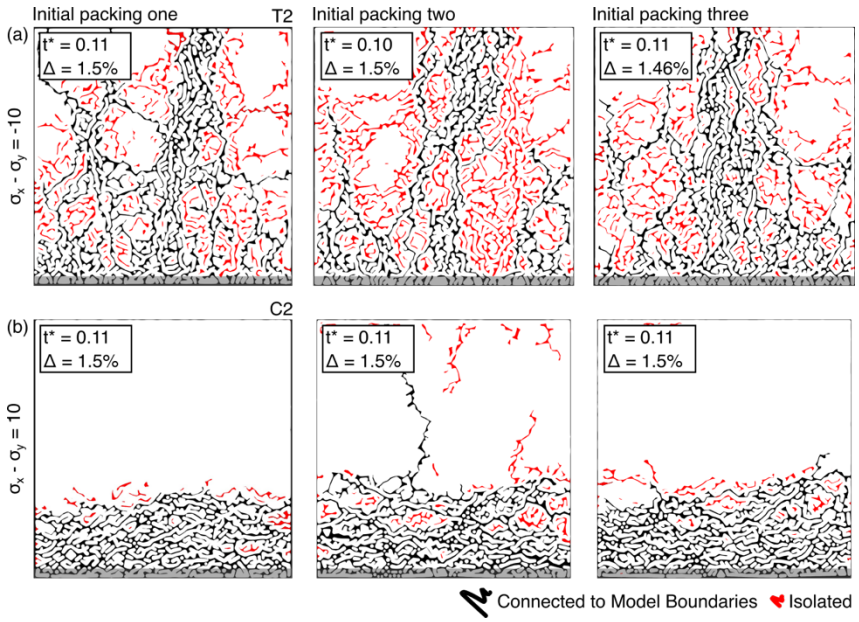

Figure S2: Comparison of simulation results for two different random initial disk packings for (a) horizontal deviatoric tension and (b) horizontal deviatoric compression. Initial packing one corresponds to models presented in Figs. 3–6 in the main text.

S3 Effects of Inertia Cracks

To find a reaction rate that results in a stable solution under differential stress, we ran simulations with varying reaction rates under horizontal compression ($(\sigma_x - \sigma_y) = 10$ MPa). These simulations had a similar setup to those in the main text except that the unreactive layer at the base of the model was excluded, the simulations were run at a higher confining pressure of 5 MPa, and ψ_m and ψ_f were 10 and 100000, respectively. The results of those simulations show that the crack density loses its dependence on Z_{max} when $Z_{max} \leq 25$ s^{-1}, indicating that inertial cracks are minimized for those Z_{max}. However, when Z_{max} is less than 25 s^{-1}, the ratio of shear to tensile cracks in the simulations increases with decreasing Z_{max} and becomes stable when Z_{max} is below 5 s^{-1} (**Fig. S2**). To minimize this effect and ensure a stable solution, we choose Z_{max} = 5 s^{-1} for the simulations in the main text. We note that a series of simulations run with constant Z_{max} but varying time step magnitudes indicate that the above dependence of the shear to tensile crack ratio on Z_{max} is independent of the time step size.

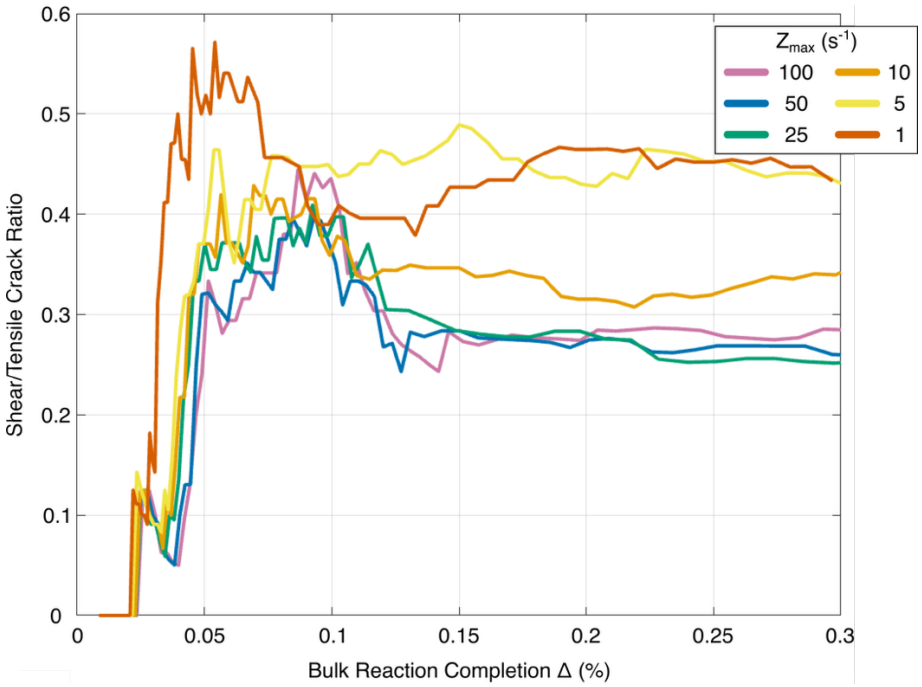

Figure S3: Ratio of shear to tensile cracks with the bulk reaction completion (Δ) for models at different maximum reaction rates. Note that, for $\Delta > 0.15\%$, the ratio of shear to tensile cracks loses its Z_{max} dependence when Z_{max} is small (≤ 5 s^{-1}).

S4 Effects of Model Dimensions

The model dimensions in this study were 5 mm × 5 mm. To test the effect of the height of the model domain, simulations were run at $(\sigma_x - \sigma_y) = 0, 2, 5$, and 10 MPa with 10-mm-high model domains (**Fig. S3**) and compared to results from the 5-mm-high models discussed in the main text. In the compressive simulations in the main text, a reacting layer characterized by spalling develops at the base of the model before the model transitions to longer tensile fractures at high angles to the base of the model when the reacting layer reaches some thickness. The models with varying aspect ratios indicate that the thickness of this layer before the transition to branching fracture increases with lateral compressive stress and the height of the model. This is consistent with previous modeling results that indicate the transition from spalling to branching depends on the domain size (*Ulven et al., 2014a; Iyer et al., 2008*) and with arguments from elasticity (*Timoshenko and Moreno, 1970*). In the 5- and 10-mm-high models under the hydrostatic condition, the branching pattern develops immediately without the development of a reacting layer. Therefore, the fracture pattern under hydrostatic stress and deviatoric tension can be thought of as an end member with a reacting layer thickness of 0.

Although the fracture style is the same in the 5- and 10-mm-high hydrostatic models, the volume of fluids channeled into the model is much larger in the 10-mm-high model because the cracks can be longer. As a result, after the first tensile cracks connect to the base of the model, the average reaction rate of the whole model becomes much faster than in the models under lateral compression. The 5-mm-high models show a model reaction rate similar to the lateral compression models because the tensile cracks are limited by the boundaries of the model. Because of this effect of model size on the flow rate, we do not directly compare the magnitude of flow rates into the model domain for each stress condition in the main text. Instead, we focus on changes in the flow rate through time.

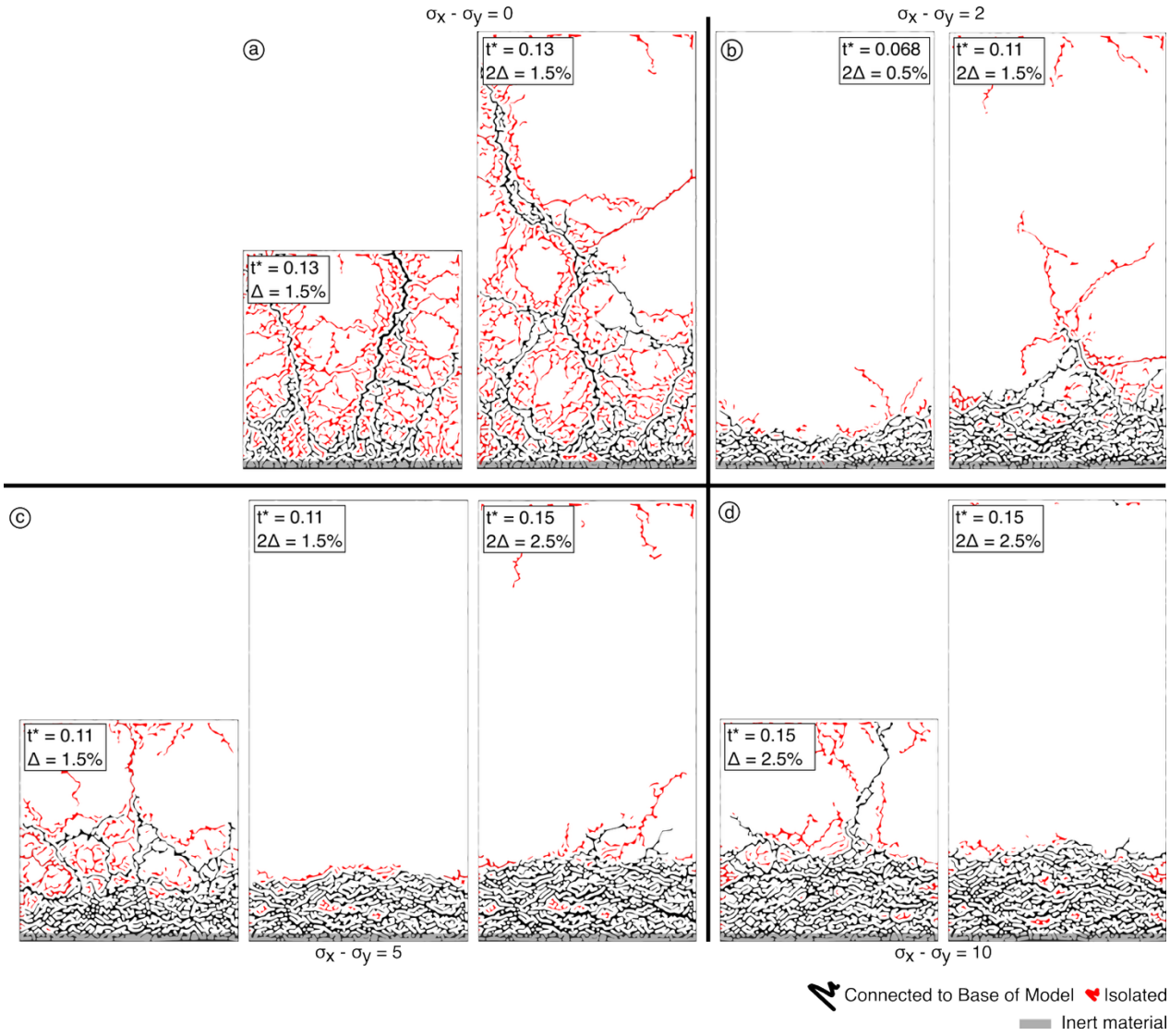

Figure S4: The effect of model domain height under (a) hydrostatic, (b) horizontal compression of 2 MPa, and (c) horizontal compression of 5 MPa, and (d) horizontal compression of 10 MPa. Square models for the hydrostatic case, the 5 MPa horizontal compression case, and the 10 MPa horizontal compression case are included for comparison. Black and red paths indicate cracks that are connected to and isolated from the model boundaries, respectively. Models run under lateral compression exhibit a fractured front at the base of the model domain before developing branching tensile cracks in the interior. With increasing lateral compression and increasing model height, the thickness of the reactive fractured layer increases prior to tensile cracking.

S5 Models with Higher Matrix Permeability

We tested the effect of permeability on the models by running simulations under deviatoric tension ($\sigma_x - \sigma_y = -10$), a hydrostatic condition ($\sigma_x - \sigma_y = 0$), and deviatoric compression ($\sigma_x - \sigma_y = 10$) with matrix permeabilities ten times higher than in the main text ($\psi_m = 10$ here). The results indicate that high matrix permeability limits spalling, leading to larger subdomains of the unreacted interior via branching. In all three simulations, spalling was much less prevalent than in the low permeability models in the main text. Less spalling is consistent with the results in **Text S3** because high permeability results in a thicker reacting layer relative to the unreacted interior, which promotes branching. In the deviatoric tension case, high

permeability also limits spalling parallel to long tensile cracks. The anticorrelation between spalling and matrix permeability was explored in *Ulven et. al. (2014b)* and our results here are consistent with what they report.

Additionally, in the hydrostatic and deviatoric tension models, the subdomains created by branching fractures were larger than in the low permeability models in the main text. This may be because there was less spalling, which encroaches on the unreacted subdomains. Alternatively, it may be because less fracture occurred in general. High matrix permeability results in low reaction-induced strain gradients. Given that cracking occurs due to strain gradients, the end result of higher matrix permeability is fewer cracks and larger subdomains. End member simulations in *Shimizu and Okamoto (2016)* indicate that very little cracking occurs when the matrix permeability is too high, and that, up to the endmember permeability, the amount of cracking decreases with increasing permeability.

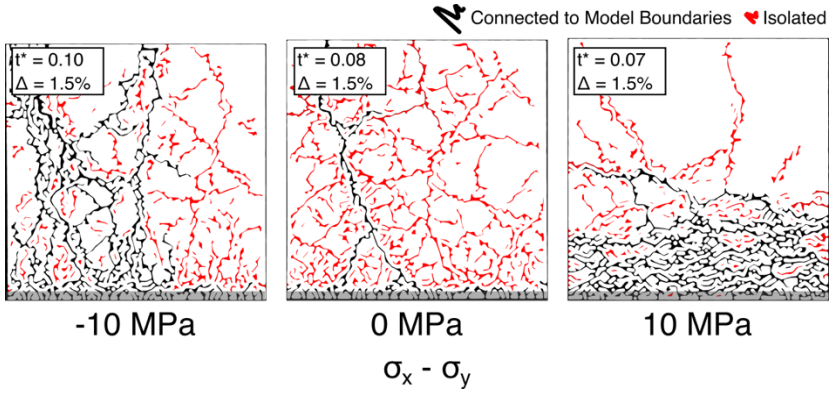

Figure S5: Simulations run with a higher matrix permeability ($\psi_m = 10$). Left: horizontal deviatoric tension. Center: hydrostatic condition. Right: horizontal deviatoric compression. Black and red paths indicate cracks that are connected to and isolated from the model boundaries, respectively.

References

Christensen, N. I.: Serpentinites, peridotites, and seismology, International Geology Review, 46, 795–816, https://doi.org/10.2747/0020-6814.46.9.795, 2004.

Iyer, K., Jamtveit, B., Mathiesen, J., Malthe-Sørenssen, A., and Feder, J.: Reaction-assisted hierarchical fracturing during serpentinization, Earth and Planetary Science Letters, 267, 503–516, https://doi.org/10.1016/j.epsl.2007.11.060, 2008.

Okamoto, A. and Shimizu, H.: Contrasting fracture patterns induced by volume-increasing and -decreasing reactions: Implications for the progress of metamorphic reactions, Earth and Planetary Science Letters, 417, 9–18, https://doi.org/10.1016/j.epsl.2015.02.015, 2015.

Shimizu, H. and Okamoto, A.: The roles of fluid transport and surface reaction in reaction-induced fracturing, with implications for the development of mesh textures in serpentinites, Contributions to Mineralogy and Petrology, 171, 1–18, https://doi.org/10.1007/s00410-016-1288-y, 2016.

Shimizu H., Murata S., and Ishida T.: Effects of Particle Number and Size Distribution on Macroscopic Mechanical Properties of Rock Models in DEM, J. Soc. Mat. Sci., Japan, 59, 219–226, https://doi.org/10.2472/jsms.59.219, 2010.

Timoshenko, P. S., Goodier, J.N.: Theory of Elasticity, third edition. McGraw-Hill, New York. ISBN 07-064720-8, 1970

Ulven, O. I., Jamtveit, B., and Malthe-Sørenssen, A.: Reaction-driven fracturing of porous rock, Journal of Geophysical Research: Solid Earth, 119, 7473–7486, https://doi.org/10.1002/2014JB011102, 2014a.

Ulven, O. I., Storheim, H., Austrheim, H., and Malthe-Sørenssen, A.: Fracture initiation during volume increasing reactions in rocks and applications for CO2 sequestration, Earth and Planetary Science Letters, 389, 132–142, https://doi.org/10.1016/j.epsl.2013.12.039, 2014b.

Zhang, L., Nasika, C., Donzé, F. V., Zheng, X., Renard, F., and Scholtès, L.: Modeling Porosity Evolution Throughout Reaction-Induced Fracturing in Rocks With Implications for Serpentinization, Journal of Geophysical Research: Solid Earth, 124, 5708–5733, https://doi.org/10.1029/2018JB016872, 2019.